# High efficiency air-bridge thermophotovoltaic cells

Bosun Roy-Layinde<sup>1</sup>, Jihun Lim<sup>2</sup>, Claire Arneson<sup>3</sup>, Stephen R. Forrest<sup>2,3,4</sup>,

Andrej Lenert<sup>\*,1</sup>

<sup>1</sup>Department of Chemical Engineering

<sup>2</sup>Department of Electrical Engineering and Computer Science

<sup>3</sup>Department of Physics

<sup>4</sup>Department of Materials Science and Engineering

University of Michigan, Ann Arbor, MI, 48109, USA

\*Corresponding author and lead contact: Andrej Lenert, <u>alenert@umich.edu</u>

©2024. This manuscript version is made available under the CC-BY-NC-ND 4.0 license <a href="https://creativecommons.org/licenses/by-nc-nd/4.0/">https://creativecommons.org/licenses/by-nc-nd/4.0/</a>

# **Summary**

Thermophotovoltaic (TPV) cells generate electricity by converting infrared radiation emitted by a hot thermal source. Air-bridge TPVs have demonstrated enhanced power conversion efficiencies by recuperating a large amount of power carried by below-bandgap (out-of-band) photons. Here, we demonstrate single-junction InGaAs(P) air-bridge TPVs that exhibit up to 44% efficiency under 1435°C blackbody illumination. The air-bridge design leads to near-unity reflectance (97-99%) of out-of-band photons for ternary and quaternary TPVs whose bandgaps range from 0.74 to 1.1 eV. These results suggest the applicability of the air-bridge cells to a range of semiconductor systems suitable for electricity generation from thermal sources found in both consumer and industrial applications, including thermal batteries.

# **Keywords**

thermophotovoltaics, air-bridge cells, photon recovery, thermal batteries

## Introduction

Thermophotovoltaics (TPVs) can take advantage of many high temperature sources to produce electricity on demand. Compared to analogous mechanical systems, TPV converters have the potential to be less expensive and more adaptable to intermittent use, which is critical to the integration of renewable energy sources. Specifically, TPVs can be combined with thermal energy storage to allow multi-day energy storage of electricity at sufficiently low cost <sup>1-6</sup> to enable a fully renewable grid. Thermal batteries based on TPV technology store surplus electrical energy from the grid by resistively heating an insulated thermal mass; they then release the stored energy by using TPVs to transform the thermal radiation emitted from the cooling mass back into electricity. Improving the efficiency and long-term stability of TPV converters is important to the deployment of such technologies.

Recent progress in TPVs has led to reported efficiencies as high as 41%<sup>7,8</sup>, albeit using very high emitter temperatures. For example, LaPotin *et al.*<sup>7</sup> demonstrated an efficiency of 41% with a III-V semiconductor tandem (1.4/1.2 eV) device using a 2400°C halogen bulb, while Tervo *et al.*<sup>8</sup> reported an efficiency of 39% with a single-junction InGaAs (0.75 eV) cell using an 1850°C protected graphite heater. The elevated power density of TPVs, which is 50-500X that of solar PV, can justify the use of such high quality III-V cells and their corresponding substrates. Nonetheless, the use of such high temperatures to maximize performance in these systems hinders the deployment of TPVs due to challenges in finding stable emitter materials and isolating the cells from contamination<sup>9–12</sup>. Recent materials screening studies<sup>13,14</sup> have identified promising emitters for ultrahigh temperature applications, however, corresponding experiments<sup>14,15</sup> have revealed

lower stability than predicted. Furthermore, system-level mitigation strategies to facilitate the use of intrinsically *unstable* emitters at such conditions have not been experimentally verified.

In this context, selecting an emitter temperature range based on the stability of commonly available emitter materials such as SiC (*e.g.*, 1200-1600 °C) is advantageous. Unfortunately, the highest TPV efficiencies reported at such emitter temperatures are currently limited to <37%, 8,16-20. A large fraction of energy losses in leading devices is attributed to parasitic absorption of below-bandgap (out-of-band) radiation. >50% of the emitted radiation is typically in this range. Our previous research has shown that introducing a nanoscale air layer between an absorber and the rear metal electrode, thus forming an air-bridge cell, can enhance the reflectance of out-of-band photons (*Rout*) to as high as 98.5% 16,19,20. When that reflected light is recaptured by the emitter, which should be feasible in scaled-up integrated TPV systems, 4 the efficiency is substantially enhanced. Towards such demonstrations, our previous research has also implemented a membrane support layer 20 to minimize mechanical failures and has demonstrated wafer-scale fabrication 19 of air-bridge back electrodes, which supports the potential of scaling up the technology. The latter was implemented using Si absorbers, but the bonding and patterning processes involved in making the air-bridge layers directly apply to other material systems.

In this work, we investigate whether translating the air-bridge architecture from ternary to quaternary group III-V absorbers (InGaAsP lattice matched to InP substrates) can enhance the efficiency within the target range of emitter temperatures. We experimentally demonstrate 43.8 ( $\pm 0.5$ ) % efficient conversion of absorbed radiation into electrical power based on current-voltage measurements under 1435 °C silicon carbide illumination combined with a calculation of absorbed

heat based on optical characterization (as in Refs.  $^{16,18,20}$ ), hereafter referred to as TPV efficiency. Supplemental Information Section 1 provides an overview of common TPV efficiency characterization techniques, including calorimetry at high view factors  $^{21}$ , and the error mitigation approaches used in this study. With future work to translate the approach to larger scales, the airbridge cells shown here have the potential to be key materials in the widespread implementation of TPV technology because of their use of single-junction cells and substantially lower emitter temperatures than in recent high-efficiency reports  $^{7,8,22}$ . This work also highlights the transferability of the air-bridge architecture with >97%  $R_{out}$  to a range of semiconductor materials.

## Results and discussion

The efficiency of TPV cells is dependent on various material and device factors, including out-of-band reflectance, material growth quality, and series resistance. Small deviations of these factors from theoretical predictions can have a large impact on efficiency, <sup>23–25</sup> which makes it challenging to specify an optimal bandgap *a priori*. To investigate these effects in air-bridge cells and optimize performance at the target emitter temperatures (1200-1600°C), we selected the following three materials to implement our cell design: In<sub>0.53</sub>Ga<sub>0.47</sub>As (0.74 eV), In<sub>0.69</sub>Ga<sub>0.31</sub>As<sub>0.67</sub>P<sub>0.33</sub> (0.9 eV) and In<sub>0.83</sub>Ga<sub>0.17</sub>As<sub>0.37</sub>P<sub>0.63</sub> (1.1 eV). The materials are commercially grown by metalorganic chemical vapor deposition (MOCVD) in the In<sub>1-x</sub>Ga<sub>x</sub>As<sub>1-y</sub>P<sub>y</sub> (InGaAsP) material system lattice-matched to (100) InP substrates.

The epitaxial materials are fabricated into cells according to the architecture in Figure 1. The fabrication steps, including transfer of the epitaxial layers from InP to the Si substrate, are described in *Experimental Procedures*. The design features a 570 nm thick air gap below the active

region that minimizes absorption at the rear metal electrode<sup>16,19</sup>. Parasitic free carrier absorption of incident radiation is also reduced using a heterojunction with a lightly doped absorber layer<sup>26</sup> and by positioning metal grids with high infrared reflectance directly over the relatively high-doped contact regions. The combination of a nanoscale air layer and a relatively high coverage of conductive rear electrodes ensures that the air-bridge thermal resistance is small compared to that of the Si substrate<sup>16</sup>. Additionally, the design includes a membrane support layer to minimize buckling of the free-standing semiconductor membrane and ensure a single cavity mode within the air layer<sup>20</sup>.

Figure 2a shows the measured spectral absorptance of the three cells at near-normal incidence along with the 1500°C blackbody spectrum. The spectra show characteristic features of free carrier absorption (<0.3 eV), Fabry-Perot cavity modes<sup>27</sup>, and inter-band transitions. When weighted to a 1500°C blackbody spectrum, the FTIR measurements yield out-of-band reflectances of  $R_{out}$  = 97.4(±0.1) %, 98.3(±0.1) % and 98.6(±0.2) % for the 0.74 eV, 0.9 eV and 1.1 eV InGaAs(P) cells, respectively. The effects of hemispherical integration and emitter temperature on  $R_{out}$  are presented in *Supplemental Information Section 2*. The slight increase in  $R_{out}$  with increasing bandgap is due to widening of the out-of-band spectral range, which diminishes the impact of free carrier absorption. These results also represent a 3% to 6% absolute increase in  $R_{out}$  compared to cells without the air bridge (see *Supplemental Information Section 3*).

The spectral management efficiency of the cells, captured by the product of the spectral efficiency (SE) and the internal quantum efficiency (IQE), is shown in Figure 2b. The three air-bridge cells (0.74, 0.9 and 1.1 eV) exhibit maximum  $SE \cdot IQE = 71.3\%$ , 73.3%, and 64.1%, respectively, for

emitter temperatures ranging from 900 to 1600°C. The choice of a lower emitter temperature range, justified by the availability of common emitter materials, is largely responsible for the lower spectral efficiency of the 1.1 eV cell. Remarkably, the 0.9 eV cell outperforms the already high spectral efficiency of the 0.74 eV cell at temperatures as low as 1200°C. Overall, these results demonstrate that the air-bridge design significantly enhances out-of-band reflectance in a range of thin-film cells, enabling spectral management efficiencies >70%.

Figure 3a shows the dark current density-voltage (J-V) characteristics of the three devices. Figure 3b shows representative J-V and power density-voltage (P-V) trends for the three water-cooled cells under illumination by a SiC emitter. Cell parameters such as the series resistance ( $R_s$ ), shunt resistance ( $R_s$ ), and dark saturation current densities are extracted<sup>28</sup> from both the dark and illuminated measurements and used as inputs in the semi-empirical cell model. Cell parameters and complete experimental data for the devices are provided in the *Supplemental Information Section 4*. The results of the model (dashed curves) agree with the measured power outputs within 5%, validating the use of the model in additional analysis.

Figure 3c shows the dependence of key electrical parameters on emitter temperature, including short-circuit current density ( $J_{SC}$ ), open circuit voltage ( $V_{OC}$ ), fill factor (FF), and maximum power point ( $P_{mpp}$ ). The  $V_{OC}$  generally increases by 100 mV with each bandgap increment from 0.74 eV to 0.9 eV (+160 meV increment) to 1.1 eV (+200 meV increment). When controlling for current density as shown in SI Section 4, all three cells exhibit similar bandgap-offset voltages (i.e., the difference between the bandgap and  $V_{OC}$ ), approaching 200-225 mV at current densities of 1 A/cm<sup>2</sup>. The fill factors are in the range of 65-75% for 0.74 eV cell and 70-85% for the other two.

FF generally decreases with emitter temperature due to series resistance losses and increases with bandgap due to higher Voc. However, the higher series resistance of the 1.1 eV cell, which can be attributed to the sensitivity of the p-type InGaAs at the metal-alloyed interface resulting in varying contact resistance<sup>29,30</sup>, produces similar FFs to those of the 0.9 eV cell.

The charge-carrier management efficiencies, captured by the product of FF and the voltage factor (VF) (*i.e.*, the ratio of the open-circuit voltage to the bandgap), approach 60% within this range of emitter temperatures for the 0.9 eV and 1.1 eV cells, outperforming the 0.74 eV where  $VF \cdot FF = 50.4 \pm 0.4\%$  at 1395°C. In comparison, the recently reported 41%-efficient tandem (1.4/1.2 eV) and 39%-efficient single junction InGaAs (0.75 eV) cells exhibited comparable values of  $VF \cdot FF = 63\%$  at 2400°C <sup>7</sup> and 59% at 1850°C (2), respectively.

Competition between spectral and carrier management produces the dependence of TPV efficiency on emitter temperature shown in Figure 4a. TPV efficiency is here defined as the ratio of  $P_{mpp}$  to the power absorbed by the cells ( $P_{abs}$ ), which is measured by FTIR characterization of the reflected power (see *Experimental Procedures* and *SI Section 1* for additional information). The efficiency of the air-bridge cells increases with emitter temperature as more incident power shifts to the inband region, before it gradually decreases due to thermalization and series resistance losses. These effects lead to an optimal operating point that shifts to higher temperatures with increasing bandgap.

All three air-bridge cells show substantial efficiency improvements compared to cells without the air bridge (see *SI Section 3*). The peak efficiency measured for the 0.74 eV cell is 36.0 ( $\pm$ 0.3) %

under 1480°C illumination, which is higher than in our previous work<sup>16</sup> due to improvements in Voc (see SI Section 5 for a detailed comparison). The 1.1 eV cell exhibits a peak efficiency of 36.1  $(\pm 0.2)$  % under 1630°C illumination. This value is expected to grow slightly at higher temperatures as shown in SI Section 5, but this cell's performance is ultimately limited by the combination of relatively high series resistance and the higher photocurrent densities characteristic of higher temperature illumination. The best-performing cell is the 0.9 eV cell, which shows a peak efficiency of 43.8 (±0.5) % under 1435°C illumination. This result represents a significant departure from the temperature-dependent efficiency of state-of-the-art (SOA) TPV cells represented by the gray band in Figure 4a (see also SI Section 6). Notably, the 0.9 eV device matches the spectral efficiency of the 0.74 eV cell while greatly increasing the carrier management efficiency as shown in Figure 4b. Relative to TPV cells reported by LaPotin et al. (1.4/1.2 eV) and Tervo et al. 8 (0.75 eV), the 0.9 eV cell shows enhanced spectral performance and comparable carrier management. We note that increasing the area of our cells from 2 mm to similar dimensions as in Refs. 7,8 without optimization of the grid architecture may introduce additional losses such as higher series resistance. Nonetheless, these efficiency results demonstrate the advantages of increasing the bandgap to improve carrier utilization while relying on the air-bridge design to manage the absorbed spectrum, rather than attempting to harvest a broader range of wavelengths using a lower bandgap device.

The highest power densities demonstrated in this work are 1.2 W/cm<sup>2</sup> and 0.91 W/cm<sup>2</sup> with the 0.74 eV and 0.9 eV cells, respectively. The measured power density is primarily limited by the view factor (*i.e.*, the net fraction of emitter thermal radiation reaching the TPV cell), which is 0.33-0.38 in our test station. Nonetheless, these results follow the general dependence of measured

power density on emitter temperature observed in recent TPV literature as shown in *SI Section 6*. Increasing the view factor increases current and power densities but it will also lower the efficiency due to series resistance losses. Assuming a view factor of 1, the validated model for the 0.9 eV cell predicts power densities of 1.7 and 1 W/cm<sup>2</sup>, and efficiencies of 38% and 40% under 1400°C and 1250°C illumination, respectively (see *SI Section 7*). In this high-view-factor case, the optimal emitter temperature decreases to mitigate the impact of series resistance losses.

The foregoing results demonstrate that >40% TPV efficiency is possible over a wide range of illumination temperatures by using the air-bridge design along with high-quality materials and an optimized bandgap. This enhanced illumination-temperature window can benefit a wide array of energy harvesting technologies, ranging from small nuclear reactors to scavenging waste heat in manufacturing processes, to large-scale stationary energy storage. Regarding the latter, the cells demonstrated here have the potential to exhibit competitive costs per unit power (CPP), while substantial reducing the cost per unit energy stored (CPE) in thermal batteries that are based on sensible heating/cooling of the storage medium (*e.g.*, graphite). The storage capacity of such batteries is approximately determined by the integral of the thermal capacitance of the medium and the TPV efficiency over the illumination-temperature window. Therefore, maintaining high TPV efficiencies over a wide temperature window can enhance the storage capacity of thermal batteries, thereby decreasing CPE and further improving competitiveness with other energy storage technologies.

#### **Conclusions**

Single-junction air-bridge cells in three absorber bandgaps, ranging from 0.74 eV to 1.1 eV, were demonstrated and characterized at moderate emitter temperatures ranging from 900 to  $1600^{\circ}\text{C}$ . For each material, we demonstrate enhanced spectral efficiency enabled by an air-bridge design that offers near unity reflectance of out-of-band radiation. Our results show that increasing the bandgap within this emitter temperature range leads to improved charge carrier utilization while the negative impact on spectral utilization is minimized because of the high out-of-band reflectance. The 0.9 eV cell exhibits the highest efficiency  $(43.8 \pm 0.5\% \text{ at } 1435^{\circ}\text{C})$  by combining a charge-carrier management efficiency of  $59.8 \pm 0.7\%$  and a spectral management efficiency of  $73.3 \pm 0.1\%$ .

## **Experimental Procedures**

## Resource availability

Lead contact

Requests for further information, resources, or materials should be directed to and will be fulfilled by the lead contact, Andrej Lenert (alenert@umich.edu).

Materials availability

The materials generated in this study are stored at the University of Michigan and can be made available upon request.

Data and code availability

Data and codes utilized in this work are available here: https://doi.org/10.7302/7qsw-je08. Additional data formats and codes can be made available upon request.

#### Material growth

The heterostructure is epitaxially grown by metalorganic chemical vapor deposition on a 600 $\mu$ m thick (100) Zn-doped InP substrate (Microlink Devices Inc., Niles, IL, USA). The epitaxial film consists of a 500nm thick Zn-doped (1 × 10<sup>17</sup> cm<sup>-3</sup>) In<sub>0.53</sub>Ga<sub>0.47</sub>As (InGaAs) etch stop layer, 100nm thick Zn-doped (1 × 10<sup>17</sup> cm<sup>-3</sup>) InP etch stop layer, 100nm thick Zn-doped (4 × 10<sup>18</sup> cm<sup>-3</sup>) In<sub>0.53</sub>Ga<sub>0.47</sub>As (InGaAs) front contact layer, 300nm Zn-doped (4 × 10<sup>18</sup> cm<sup>-3</sup>) InP front window layer, Te-doped (1 × 10<sup>17</sup> cm<sup>-3</sup>) absorber layer, 50 nm thick Te-doped (3 × 10<sup>18</sup> cm<sup>-3</sup>) InP rear window layer, 1 $\mu$ m thick Te-doped (1 × 10<sup>17</sup> cm<sup>-3</sup>) InP buffer layer, and 100nm thick Te-doped (1 × 10<sup>18</sup> cm<sup>-3</sup>) InGaAs rear contact layer. The 1 $\mu$ m thick Te-doped InP layer serves as an additional buffer layer to strengthen the mechanical structure and minimizing buckling of the air

bridge membrane<sup>20</sup>. The thicknesses of the absorber layers are  $2\mu m$  for  $In_{0.53}Ga_{0.47}As$  and  $In_{0.69}Ga_{0.31}As_{0.67}P_{0.33}$ , and  $1.5~\mu m$  thick for  $In_{0.83}Ga_{0.17}As_{0.37}P_{0.63}$ .

#### **Fabrication**

The epitaxial samples and a Si wafer are plasma cleaned to remove residual organic material and then soaked in buffered HF for 90 seconds to remove the native surface oxides. All layers are photolithographically patterned with SPR 220 3.0 photoresist (Kayaku Advanced Material Inc., Westborough, MA). The rear contact grids (10nm Ti / 550nm Au) are deposited by electron-beam evaporation in a chamber with a base pressure of  $4x10^{-6}$  torr. The devices are 2 mm squares with 20 μm wide on a 80 μm pitch conducting grid lines. The sample is soaked in 1:1:8 H<sub>3</sub>PO<sub>4</sub>:H<sub>2</sub>O<sub>2</sub>:H<sub>2</sub>O for 20s to remove the 100 nm thick InGaAs rear contact layer between the grid lines. The Au-patterned epitaxial membranes are transferred to a Au-coated Si wafer via cold-weld bonding using an EVG 510 wafer bonder for 10 minutes under heat (150°C) and pressure (8 MPa). The InP substrates are selectively removed by wet etching by soaking in HCl:H<sub>2</sub>O (1:1) for 12 h. This method is compatible with non-destructive epitaxial lift-off used to reduce cost (11). Alternating soaks in InGaAs (1:1:8 H<sub>3</sub>PO<sub>4</sub>:H<sub>2</sub>O<sub>2</sub>:H<sub>2</sub>O) and InP (1:1 HCl:H2O) solutions are used to etch the device mesas. The front contact grids (10 nm Pt / 10 nm Ti / 15 nm Pt / 5000 nm Au) are deposited by electron-beam deposition. Finally, the sample is soaked for 20s in a 1:1:8 H<sub>3</sub>PO<sub>4</sub>:H<sub>2</sub>O<sub>2</sub>:H<sub>2</sub>O solution to remove the 100nm thick InGaAs front contact between the grid lines. We note that photolithography typically accounts for a small fraction of the overall cost relative to the growth substrate<sup>31</sup>.

### Cell optical characterization

The reflectance of each cell is measured using a Cary 670-IR spectrometer equipped with a Cary 620 IR microscope (Agilent Technologies, CA). Near- and mid- IR measurements are taken with quartz and KBr beam splitters, respectively, and a cooled MCT detector. The measurement covers incidence angles ranging from 18 to 41°. FTIR measurements are used to calculate out-of-band reflectance ( $R_{out}$ ), which is the average reflectance when weighted to an emitter spectrum.

$$R_{out} = \frac{\int_0^{E_g} R(E) \cdot E \cdot b(E, T_h) dE}{\int_0^{E_g} E \cdot b(E, T_h) dE}$$

where  $E_g$  is the cell's bandgap, E is the photon energy,  $b(E, T_h)$  is the blackbody spectral photon flux, R(E) is the measured spectral reflectance of the cell, and  $T_h$  is the emitter temperature.

#### Emitter optical characterization

Thermal emission spectra for the SiC emitters (SLS203L, Thorlabs, NJ; White-Rodgers 767A-377) are calibrated to a real blackbody source (IR-564, Infrared Systems Development Corp., FL) whose blackbody emissivity is > 0.99 according to manufacturer specifications. Emission from SiC is collimated by an off-axis parabolic mirror and directed through the external port of the Nicolet iS50 FTIR spectrometer. Linear interpolation removes H<sub>2</sub>O and CO<sub>2</sub> absorption in the spectral ranges  $2.5-2.8 \,\mu\text{m}$  and  $5-7.6 \,\mu\text{m}$ . The emission spectra shown in *SI Section 8* are compared to a blackbody curve, resulting in an average thermal emittance of 0.96.

#### Spectral efficiency (SE) calculation

The spectral efficiency is calculated according to:

$$SE = \frac{E_g \cdot \int_{E_g}^{\infty} \varepsilon_{eff}(E) \cdot b(E, T_h) dE}{\int_{0}^{\infty} \varepsilon_{eff}(E) \cdot E \cdot b(E, T_h) dE}$$

where  $b(E, T_h)$  is the spectral photon flux,  $\varepsilon_{eff}(E) = \frac{\varepsilon_h \varepsilon_c}{\varepsilon_h + \varepsilon_c - \varepsilon_h \varepsilon_c}$  is the effective emissivity of the emitter-cell pair ( $\varepsilon_h$  is the emissivity of the emitter, and  $\varepsilon_c$  is the emissivity of the cell). The effective emissivity follows  $\varepsilon_{eff} \approx \varepsilon_c$  since  $\varepsilon_h$  approaches 1 in this study (see Ref. 18 for additional discussion). Specifically, changing  $\varepsilon_h$  from 0.96 to 1 has a negligible effect on  $\varepsilon_{eff}$  (given a representative emissivity of the cell). Therefore, effects related to non-ideal absorption by the emitter, such as secondary reflections, are negligible.

## External quantum efficiency (EQE) characterization

The EQE of each cell is measured using a Xe-arc lamp (Oriel 6285) and a monochromator (SpectraPro 300i), chopped at 200 Hz. The chopped light is coupled to a fiber (ThorLabs M118L03) that is aligned to illuminate an under-filled portion of the device active area at an incidence angle of approximately 15°. The lamp spectrum is calibrated using a reference InGaAs detector calibrated from 600 to 1700 nm (Hamamatsu G10899). The device photocurrent is measured using a lock-in amplifier (Stanford Research Systems SR830), from 800 to 1700 nm with a 5 nm step size.

### View factor calculation

The view factor  $F_v$  is determined (as previously  $^{16,17,19,20}$ ) from the measured  $J_{ph}$  according to:

$$J_{ph} = F_v \cdot q \cdot \int_{E_q}^{\infty} \varepsilon_{eff}(E) / \varepsilon_c(E) \cdot EQE(E) \cdot b(E, T_h) dE$$

where *EQE* is the measured external quantum efficiency shown in *SI Section 2*. The calculated apparent view factors are 0.38, 0.37 and 0.33 for the 0.74 eV, 0.9 eV and 1.1 eV air-bridge devices, respectively. Differences in view factor across experiments are due to the manual positioning of the cells near the emitter.

#### Cell model

The current-voltage characteristics of the cells are modeled as previously using a two-diode model<sup>28</sup>, which describes different rates of recombination in the quasi-neutral ( $J_{01}$ ) and depleted regions ( $J_{02}$ ). Cell parameters such as the  $J_{01}$ ,  $J_{02}$ , series resistance  $R_s$  and shunt resistance  $R_{sh}$  are extracted from the dark and illuminated current measurements at 25°C. The optical properties of the cells are modeled as previously using a transfer matrix method that can determine the electric field distribution within the layers. The absorption coefficients ( $\alpha$ ) of the alloys are modeled using a piece-wise function.

#### Efficiency characterization

TPV efficiency  $\eta_{TPV}$  is calculated as the ratio of the maximum power produced  $P_{mpp}$  to the power absorbed  $P_{abs}$  by the cell:

$$\eta_{TPV} = \frac{P_{mpp}}{P_{abs}}$$

The maximum power  $P_{mpp}$  is determined from the current density-voltage (*J-V*) characteristics which are measured using a Keithley 2401 Source Measuring Unit (SMU) in the 4-wire sensing mode. The experimental test station is illustrated in *SI Section 8*. The absorbed power  $P_{abs}$  is quantified as the difference between the incident and reflected power on the cell. The reflected

power  $P_{ref}$  is determined by spectral integration of the product of the cell's effective reflectance and the incident power:

$$P_{ref} = F_v \int_0^\infty (1 - \varepsilon_{eff}(E)) \cdot E \cdot b(E, T_h) \ dE$$

## Error propagation

Uncertainty in the reported experimental quantities is evaluated based on propagation of the following errors: variance (using a t-distribution with a 95% confidence interval), instrument error and resolution error. All errors are assumed to be uncorrelated.

## Acknowledgments

This material is based upon work supported by the National Science Foundation under Grant Numbers 2018572 and 2144662 and the Army Research Office (ARO) under Grant Number W911-NF-17-0312. B.R.L. and A.L. acknowledge support from Rich and Gabrielle Lesser, and the Gordon & Betty Moore Foundation.

## **Author contributions**

B.R.L. and J.L. designed and fabricated the cells and performed the simulations. B.R.L., J.L. and C.A. carried out the cell characterization experiments. S.R.F and A.L. supervised the project and analyzed the data. All authors contributed to writing the paper.

# **Declaration of interests**

The authors have a patent related to this work. A.L. is a scientific advisory board member of Antora Energy.

#### References

- 1. Ziegler, M.S., Mueller, J.M., Pereira, G.D., Song, J., Ferrara, M., Chiang, Y.M., and Trancik, J.E. (2019). Storage Requirements and Costs of Shaping Renewable Energy Toward Grid Decarbonization. Joule *3*, 2134–2153. 10.1016/j.joule.2019.06.012.
- 2. Sepulveda, N.A., Jenkins, J.D., Edington, A., Mallapragada, D.S., and Lester, R.K. (2021). The design space for long-duration energy storage in decarbonized power systems. Nat Energy *6*, 506–516. 10.1038/s41560-021-00796-8.
- 3. Albertus, P., Manser, J.S., and Litzelman, S. (2020). Long-Duration Electricity Storage Applications, Economics, and Technologies. Joule *4*, 21–32. https://doi.org/10.1016/j.joule.2019.11.009.
- 4. Amy, C., Seyf, H.R., Steiner, M.A., Friedman, D.J., and Henry, A. (2019). Thermal energy grid storage using multi-junction photovoltaics. Energy Environ Sci *12*, 334–343. 10.1039/c8ee02341g.
- 5. Henry, A., Prasher, R., and Majumdar, A. (2020). Five thermal energy grand challenges for decarbonization. Preprint at Nature Research, 10.1038/s41560-020-0675-9 10.1038/s41560-020-0675-9.
- 6. Datas, A., López-Ceballos, A., López, E., Ramos, A., and del Cañizo, C. (2022). Latent heat thermophotovoltaic batteries. Joule *6*, 418–443. 10.1016/J.JOULE.2022.01.010.
- 7. LaPotin, A., Schulte, K.L., Steiner, M.A., Buznitsky, K., Kelsall, C.C., Friedman, D.J., Tervo, E.J., France, R.M., Young, M.R., Rohskopf, A., et al. (2022). Thermophotovoltaic efficiency of 40%. Nature 604, 287–291. 10.1038/s41586-022-04473-y.
- 8. Tervo, E.J., France, R.M., Friedman, D.J., Arulanandam, M.K., King, R.R., Narayan, T.C., Luciano, C., Nizamian, D.P., Johnson, B.A., Young, A.R., et al. (2022). Efficient and scalable GaInAs thermophotovoltaic devices. Joule *6*, 2566–2584. 10.1016/j.joule.2022.10.002.
- 9. Sakakibara, R., Stelmakh, V., Chan, W.R., Ghebrebrhan, M., Joannopoulos, J.D., Soljačić, M., and Čelanović, I. (2019). Practical emitters for thermophotovoltaics: A review. J Photonics Energy *9*. 10.1117/1.JPE.9.032713.
- 10. Licht, A., Pfiester, N., DeMeo, D., Chivers, J., and Vandervelde, T.E. (2019). A Review of Advances in Thermophotovoltaics for Power Generation and Waste Heat Harvesting. MRS Adv 4, 2271–2282. 10.1557/adv.2019.342.
- 11. Burger, T., Sempere, C., Roy-Layinde, B., and Lenert, A. (2020). Present Efficiencies and Future Opportunities in Thermophotovoltaics. Joule *4*, 1660.
- 12. Vaidhyanathan Krishnamurthy, G., Chirumamilla, M., Krekeler, T., Ritter, M., Raudsepp, R., Schieda, M., Klassen, T., Pedersen, K., Petrov, A.Yu., Eich, M., et al. Iridium-Based Selective Emitters for Thermophotovoltaic Applications. Advanced Materials *n/a*, 2305922. https://doi.org/10.1002/adma.202305922.
- 13. Dias, M.R.S., Gong, T., Duncan, M.A., Ness, S.C., McCormack, S.J., Leite, M.S., and Munday, J.N. (2023). Photonics roadmap for ultra-high-temperature thermophotovoltaics. Joule. https://doi.org/10.1016/j.joule.2023.08.015.
- 14. McSherry, S., Webb, M., Kaufman, J., Deng, Z., Davoodabadi, A., Ma, T., Kioupakis, E., Esfarjani, K., Heron, J.T., and Lenert, A. (2022). Nanophotonic control of thermal emission under extreme temperatures in air. Nat Nanotechnol *17*, 1104–1110. 10.1038/s41565-022-01205-1.

- 15. Gong, T., Duncan, M.A., Karahadian, M., Leite, M.S., and Munday, J.N. (2023). Broadband Superabsorber Operating at 1500 °C Using Dielectric Bilayers. ACS Applied Optical Materials *1*, 1615–1619. 10.1021/acsaom.3c00229.
- 16. Fan, D., Burger, T., McSherry, S., Lee, B., Lenert, A., and Forrest, S.R. (2020). Near-perfect photon utilization in an air-bridge thermophotovoltaic cell. Nature *586*, 237–241. 10.1038/s41586-020-2717-7.
- 17. Burger, T., Roy-Layinde, B., Lentz, R., Berquist, Z.J., Forrest, S.R., and Lenert, A. (2022). Semitransparent thermophotovoltaics for efficient utilization of moderate temperature thermal radiation. Proceedings of the National Academy of Sciences *119*, e2215977119. 10.1073/pnas.2215977119.
- 18. Omair, Z., Scranton, G., Pazos-Outón, L.M., Xiao, T.P., Steiner, M.A., Ganapati, V., Peterson, P.F., Holzrichter, J., Atwater, H., and Yablonovitch, E. (2019). Ultraefficient Thermophotovoltaic Power Conversion by Band-Edge Spectral Filtering. Proc. Natl. Acad. Sci. U. S. A. *116*, 15356.
- 19. Lee, B., Lentz, R., Burger, T., Roy-Layinde, B., Lim, J., Zhu, R.M., Fan, D., Lenert, A., and Forrest, S.R. (2022). Air-Bridge Si Thermophotovoltaic Cell with High Photon Utilization. ACS Energy Lett 7, 2388–2392. 10.1021/acsenergylett.2c01075.
- 20. Lim, J., Roy-Layinde, B., Liu, B., Lenert, A., and Forrest, S.R. (2023). Enhanced Photon Utilization in Single Cavity Mode Air-Bridge Thermophotovoltaic Cells. ACS Energy Lett 8, 2935–2939. 10.1021/acsenergylett.3c00720.
- 21. López, E., Artacho, I., and Datas, A. (2023). Thermophotovoltaic conversion efficiency measurement at high view factors. Solar Energy Materials and Solar Cells *250*, 112069. https://doi.org/10.1016/j.solmat.2022.112069.
- 22. Chemisana, D., Teixidó, O., and Vaillon, R. (2023). Silicon Vertical Multijunction Cell for Thermophotovoltaic Conversion. ACS Energy Lett *8*, 3520–3525. 10.1021/ACSENERGYLETT.3C01168.
- 23. Bauer, T. (2011). Thermophotovoltaics: basic principles and critical aspects of system design (Springer Berlin Heidelberg) 10.1007/978-3-642-19965-3.
- 24. Song, J., Han, J., Choi, M., and Lee, B.J. (2022). Modeling and experiments of near-field thermophotovoltaic conversion: A review. Solar Energy Materials and Solar Cells *238*, 111556. 10.1016/J.SOLMAT.2021.111556.
- 25. Roux, B., Lucchesi, C., Perez, J.-P., Chapuis, P.-O., and Vaillon, R. (2024). Main performance metrics of thermophotovoltaic devices: analyzing the state of the art. J Photonics Energy *14*, 42403. 10.1117/1.JPE.14.042403.
- 26. Lim, J., and Forrest, S.R. (2023). Limits to the Energy-Conversion Efficiency of Air-Bridge Thermophotovoltaics. Phys Rev Appl *19*, 34099. 10.1103/PhysRevApplied.19.034099.
- 27. Burger, T., Fan, D., Lee, K., Forrest, S.R., and Lenert, A. (2018). Thin-Film Architectures with High Spectral Selectivity for Thermophotovoltaic Cells. ACS Photonics *5*, 2748–2754. 10.1021/acsphotonics.8b00508.
- 28. Roy-Layinde, B., Burger, T., Fan, D., Lee, B., McSherry, S., Forrest, S.R., and Lenert, A. (2022). Sustaining efficiency at elevated power densities in InGaAs airbridge thermophotovoltaic cells. Solar Energy Materials and Solar Cells *236*, 111523. https://doi.org/10.1016/j.solmat.2021.111523.
- 29. Lin, J.C., Yu, S.Y., and Mohney, S.E. (2013). Characterization of low-resistance ohmic contacts to n- and p-type InGaAs. J Appl Phys *114*, 044504. 10.1063/1.4816097.

- 30. Crook, A.M., Lind, E., Griffith, Z., Rodwell, M.J.W., Zimmerman, J.D., Gossard, A.C., and Bank, S.R. (2007). Low resistance, nonalloyed Ohmic contacts to InGaAs. Appl Phys Lett *91*, 192114. 10.1063/1.2806235.
- 31. Ward, J.S., Remo, T., Horowitz, K., Woodhouse, M., Sopori, B., VanSant, K., and Basore, P. (2016). Techno-economic analysis of three different substrate removal and reuse strategies for III-V solar cells. Progress in Photovoltaics: Research and Applications *24*, 1284–1292. https://doi.org/10.1002/pip.2776.

### **Figure Captions**

**Figure 1. High performance cell design in three absorber materials.** The absorber layer is 2 μm thick for both the 0.74 eV (In<sub>0.53</sub>Ga<sub>0.47</sub>As) and the 0.9 eV cells (In<sub>0.69</sub>Ga<sub>0.31</sub>As<sub>0.67</sub>P<sub>0.33</sub>), and 1.5 μm thick for the 1.1 eV (In<sub>0.83</sub>Ga<sub>0.17</sub>As<sub>0.37</sub>P<sub>0.63</sub>) cell. A 570 nm thick air-bridge layer is situated between the active layers of the InP-based PV cell and the rear Au mirror to enhance backside reflectance and recovery of out-of-band photons.

Figure 2. Optical characterization of the air-bridge cells. (a) Experimental absorptance (= 1 - reflectance) measured by FTIR for the 0.74 eV (purple), 0.9 eV (orange) and 1.1 eV (green) air-bridge cells. (b) Spectral management efficiency ( $SE \cdot IQE$ ) for the three cells *versus* emitter temperature in the range of 900°C to 1600°C.

Figure 3. Electrical characterization of the air-bridge cells. (a) Dark current density-voltage characteristics for the 0.74 eV (purple), 0.9 eV (orange) and 1.1 eV (green) air-bridge cells. (b) Current and power density *versus* voltage for the three water-cooled cells under illumination at conditions corresponding to their maximum efficiencies. (c) Variation of short circuit current density (Jsc), open circuit voltage (Voc), fill factor (FF), maximum power point (Pmpp), and carrier management efficiency ( $VF \cdot FF$ ) *versus* emitter temperature (from 900 to 1600 °C) for the three cells. The results of the cell model (dashed curves) agree with measured power outputs.

Figure 4. Efficiency of the air-bridge cells. (a) Efficiency of air-bridge cells as a function of emitter temperature  $(T_h)$ . The gray band captures the performance of state-of-the-art (SOA) TPV cells (see *SI Section 6* for more information about the trendline). Results of the model (dashed curves) agree with experimental data. (b) Spectral management  $(SE \cdot IQE)$  vs. carrier management  $(VF \cdot FF)$  for the air bridge cells at their maximum efficiencies. Star markers signify the best previously reported efficiencies: blue<sup>7</sup> and black<sup>8</sup>.

# **Supplemental Information**

- 1. Overview of TPV efficiency characterization techniques
- 2. Optical properties of the air-bridge cells
- 3. Comparison to cells without an air bridge
- 4. Cell parameters and complete I-V experimental data
- 5. Additional analysis of the 0.74 eV and 1.1 eV cells
- 6. Comparison to state-of-the-art TPV devices
- 7. High view factor simulation for the 0.9 eV cell
- 8. Emitter and cell characterization test station

## S1. Overview of TPV efficiency characterization techniques

Efficiency characterization techniques can be broadly categorized as (A) high view-factor calorimetry (as in Refs. S1 and S2)<sup>S1,S2</sup>, (B) low view-factor calorimetry (as in Refs. S3 and S4)<sup>S3,S4</sup>, (C) based on measurement of radiative properties (as in our work and Refs. S3-S7)<sup>S3-S7</sup>. Each technique has its own general strengths (+) and weaknesses (-) as discussed below. Specific factors and strategies used to mitigate the weaknesses of the technique C used in this article are also described.

### A) high view-factor (>0.9) calorimetry:

- + captures the angular dependence of radiative exchange, as well as the effects of multiple reflections between the cell and the emitter.
- + accounts for series resistance losses associated with higher photocurrent levels.
- + accounts for possible *operando* variations in radiative properties.
- difficult to protect the cell from potential deposition of evaporated emitter material.
- not widely implemented. To our knowledge, this technique appears to only have been applied by López (Ref. S1) and Swanson (Ref. S2).
- involves possible sources of additional error (see list in B)

### B) low view-factor calorimetry (as in Refs. S3 and S4):

- + accounts for possible *operando* variations in radiative properties.
- + windows can be used to protect the cell from deposition of evaporated emitter material.
- + has been shown to agree with technique C (see Refs. S3 and S4).
- does not fully capture the angular dependence of the radiative exchange between the cell and the emitter because of the restricted emitter solid angle.
- does not fully account for series resistance losses associated with higher photocurrent levels.
- involves a range of possible sources of error associated with indirect heating of the stage, mixed parasitic heating and cooling effects of the electrical probes, and calibration of the calorimeter (e.g., heat flux sensor<sup>3,8</sup>). Corrections for these potential sources of error have not been consistently applied in the TPV literature.

#### C) emittance and reflectance measurement (as here and in Refs. S3-S7):

- + does not require calorimeter calibration or corrections for parasitic heating/cooling of the experimental apparatus.
- + has been shown to agree with technique B (see Refs. S3 and S4).
- + readily applied to low TRL cells characteristic of academic research.
- does not fully capture the angular dependence of the radiative exchange between the cell and the emitter because of the restricted solid angle occupied by the emitter. To mitigate this, we use the validated model to show the effect of hemispherical integration on efficiency in SI Section 2.
- does not account for possible in-operando variations in radiative properties. To mitigate this, we (i) measure the spectral emittance of the emitter in-operando (see *SI Section 8*), (ii) manage the temperature of cell to between 23 and 32 °C to minimize the effects of bandgap narrowing, (iii) ensure that the radiative properties before and after testing are consistent.
- does not fully account for series resistance losses associated with higher photocurrent levels. To mitigate this, we use the validated cell model to show the effect of increasing the view factor on efficiency in SI Section 7.

## S2. Optical properties of the air-bridge cells

## S2.1. Validation of optical model against experiments

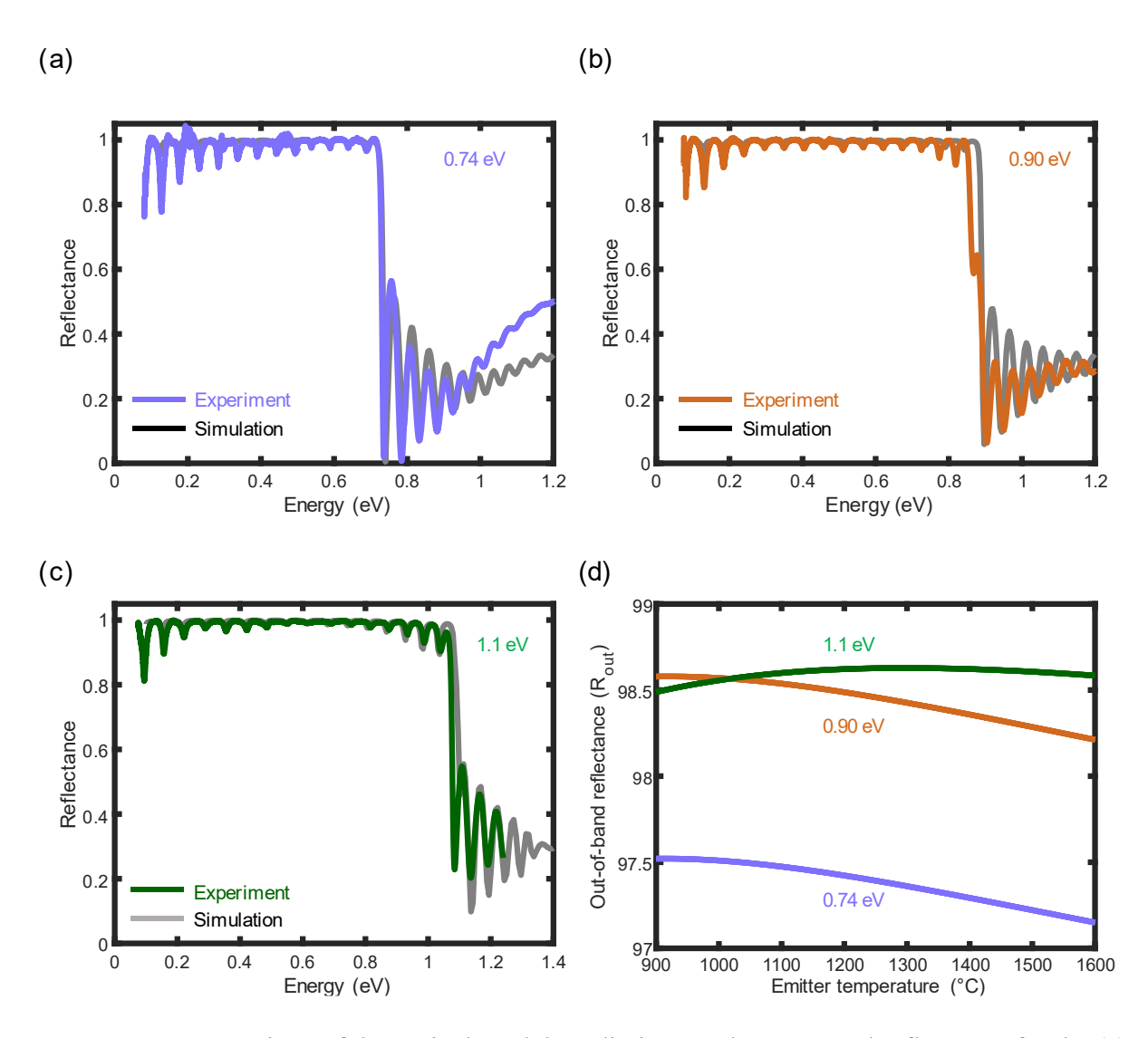


**Figure S2.1.** A comparison of the optical model predictions to the measured reflectance for the (a) 0.74 eV, (b) 0.9 eV and (c) 1.1 eV air-bridge cells. The results of the model agree with measurements, validating the use of the optical model in additional analysis. (d) Out-of-band reflectance ( $R_{\text{out}}$ ) versus emitter temperature for the three cells.

# S2.2. Effects of hemispherical integration on reflectance and efficiency:

**Table S2.2.** Simulated angular dependence of out-of-band reflectance and efficiencies for the (a) 0.74 eV, (b) 0.9 eV, and (c) 1.1 eV air-bridge cells at their respective optimal emitter temperatures.

(a) 0.74 eV

Integration angle (°)	Out-of-band reflectance	Peak efficiency (%)
	(%)	
15 (single angle)	97.5	36.7
0 to 60	97.4	36.6
0 to 90	97.2	36.2

(b) 0.9 eV

Integration angle (°)	Out-of-band reflectance	Peak efficiency (%)	
	(%)		
15 (single angle)	98.5	44.1	
0 to 60	98.5	44.1	
0 to 90	98.3	43.4	

(c) 1.1 eV

Integration angle (°)	Out-of-band reflectance	Peak efficiency (%)	
	(%)		
15 (single angle)	98.8	38.4	
0 to 60	98.7	37.6	
0 to 90	98.5	36.4	

# S2.3 External quantum efficiency (EQE):

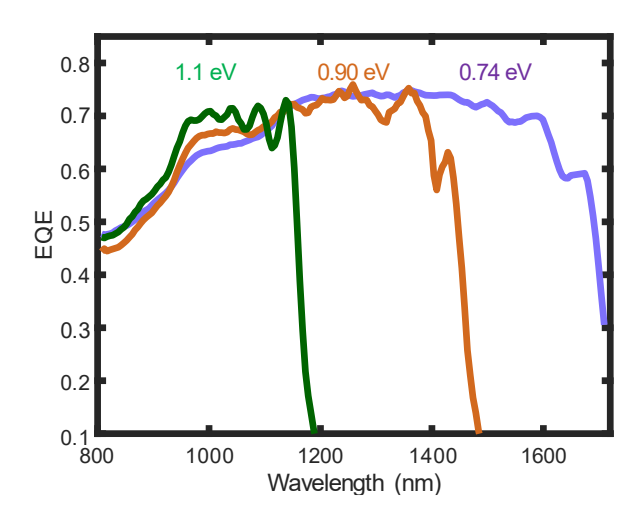


**Figure S2.3.** EQE measurements for the 0.74 eV, 0.9 eV and 1.1 eV air-bridge cells. These results correspond to an internal quantum efficiency (IQE) of ~98%.

## S3. Comparison to cells without an air bridge

TPV cells without an air bridge, also known as cells with planar Au back surface reflectors (Au-BSR), were fabricated in all three bandgaps. These cells are the same size as the air-bridge cells.

## **S3.1 Surface profilometry**

The figure below compares the surface profile of the air-bridge cells to the Au-BSR cells, highlighting the flatness of the air-bridge architecture.

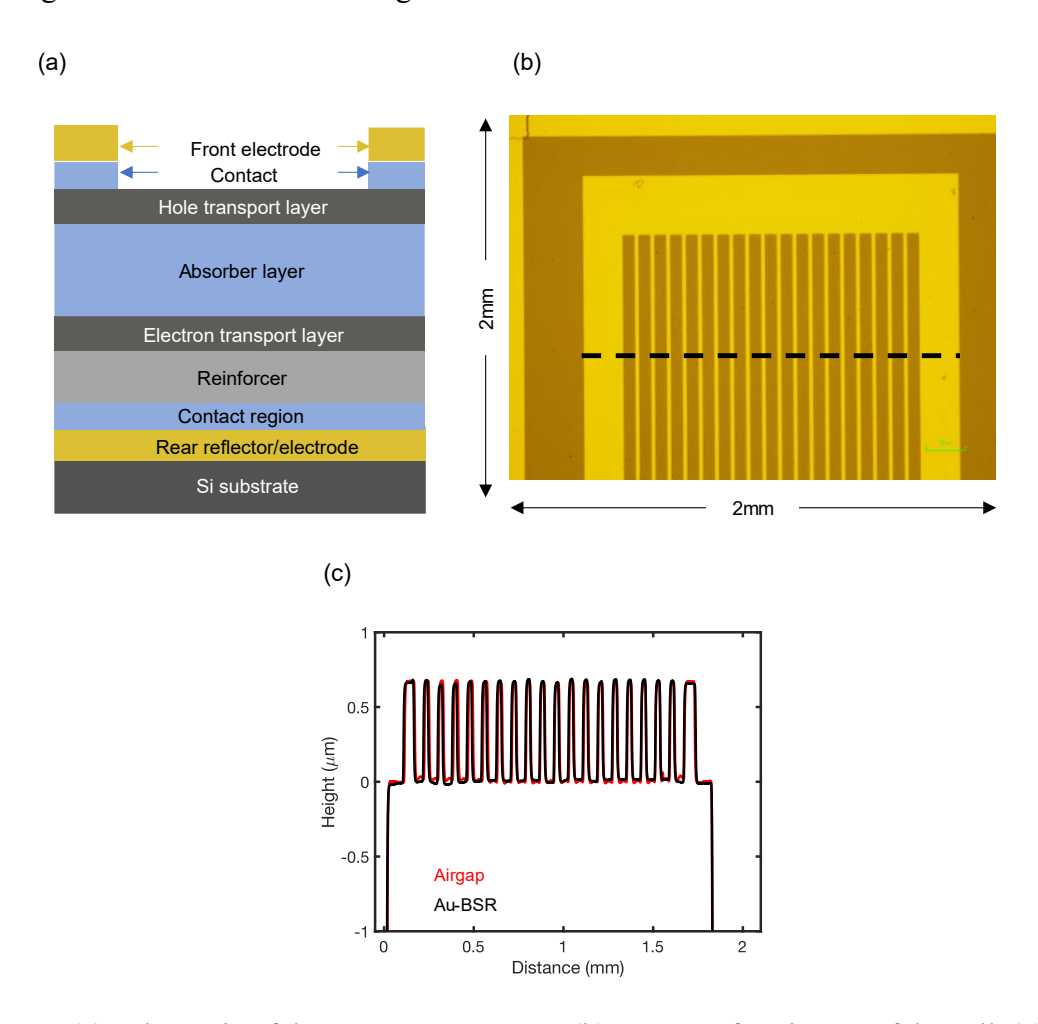


**Figure S3.1.** (a) Schematic of the Au-BSR structure. (b) Front surface image of the cell. (c) Surface profilometer scan of the Au-BSR and air-bridge cells highlighting its flatness.

# S3.2. Cross-section imaging

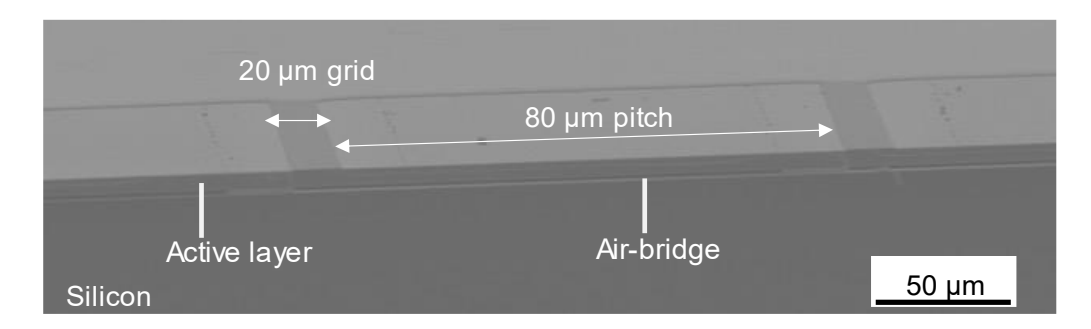


**Figure S3.2.** SEM of the TPV cell showing the air-bridge suspension between the active layer and the silicon substrate.

## S3.3. Optical and electrical characterization of Au-BSR cells

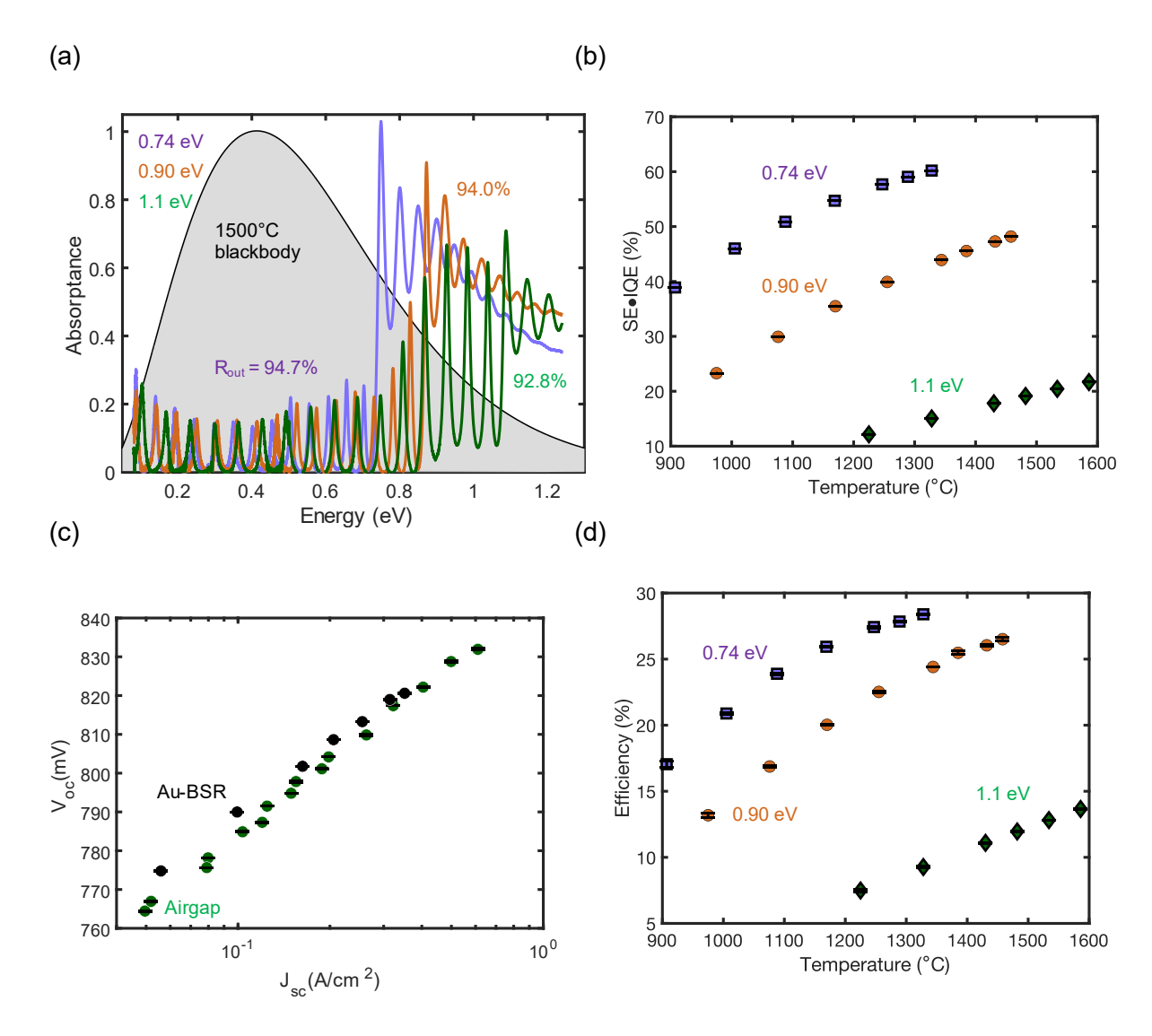


**Figure S3.3.** (a) Absorptance of the 0.74 eV (purple), 0.9 eV (orange) and 1.1 eV (green) Au-BSR cells measured using FTIR. Weighted to a 1500°C blackbody emission spectrum,  $R_{out} = 94.7 \pm 0.2\%$ , 94.0  $\pm$  0.1% and 92.8  $\pm$  0.2%, respectively. (b) Spectral management efficiencies of the Au-BSR cells as a function of emitter temperature. (c) *Voc vs. Jsc* comparing 1.1 eV Au-BSR and airbridge cells. (d) TPV efficiencies of the Au-BSR cells *versus* emitter temperature.

## S4. Cell parameters and complete I-V experimental data

## **S4.1.** Equivalent circuit parameters:

Table S4.1. Extracted cell characteristics from both dark and illuminated current measurements.

T <sub>h</sub> (°C)	$J_{01}$ (mA/cm <sup>2</sup> )	$J_{02}$ (mA/cm <sup>2</sup> )	$R_s$ (m $\Omega$ .cm <sup>2</sup> )	$R_{sh}$ (k $\Omega$ .cm <sup>2</sup> )
0.74 eV	1.47 x 10 <sup>-9</sup>	1.97 x 10 <sup>-6</sup>	30	11
0.9 eV	6.45 x 10 <sup>-12</sup>	3.39 x 10 <sup>-8</sup>	40	825
1.1 eV	9.77 x 10 <sup>-15</sup>	2.04 x 10 <sup>-9</sup>	60	260

## S4.2. Current-voltage (*J-V*) characteristics:

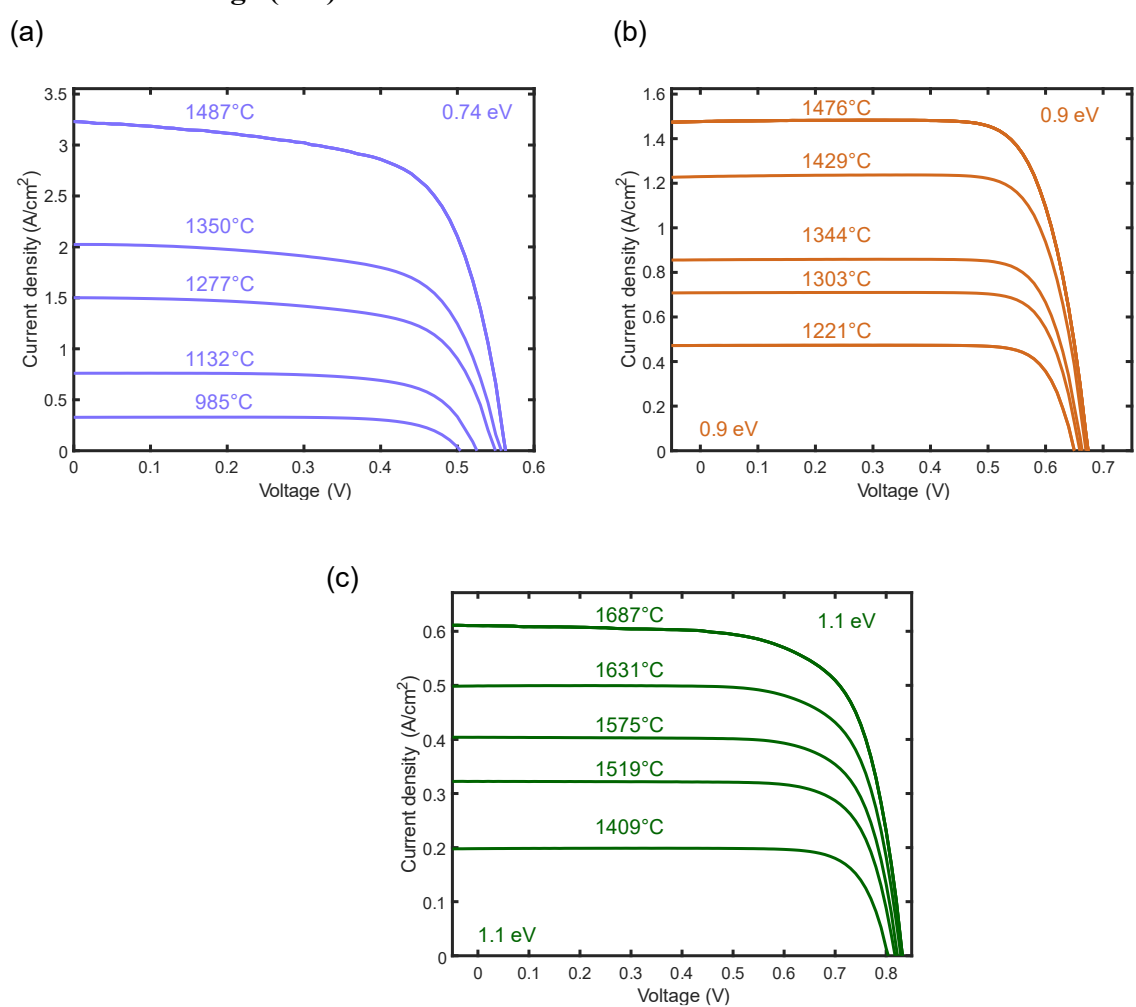


**Figure S4.2**. Experimental J-V characteristics under illumination for the (a) 0.74 eV, (b) 0.9 eV and (c) 1.1 eV air-bridge cells.

**Table S4.2.** Variation in measured open-circuit voltage (Voc), short-circuit current (Jsc), fill factor (FF), and power density ( $P_{mpp}$ ) versus emitter temperature ( $T_h$ ) for the (a) 0.74 eV, (b) 0.9 eV, and (c) 1.1 eV air-bridge cells.

(a) 0.74 eV

T <sub>h</sub> (°C)	J <sub>SC</sub> (mA/cm <sup>2</sup> )	V <sub>OC</sub> (mV)	FF (%)	$P_{mpp}$ $(mW/cm^2)$
745	51.30	449.53	72.96	16.83
830	107.73	472.74	74.85	38.12
909	196.49	490.06	74.59	71.82
985	327.80	504.02	73.58	121.56
1024	416.99	510.26	72.82	154.94
1060	514.95	516.21	72.22	191.97
1091	610.84	520.2	72.47	230.27
1132	759.76	525.52	70.07	279.76
1163	887.62	529.57	70.31	330.48
1203	1079.33	537.52	68.24	395.92
1235	1250.00	544.23	68.35	464.97
1277	1501.83	549.73	66.71	550.78
1313	1743.41	552.99	66.51	641.2
1350	2023.82	557.41	66.8	747.66
1271	1460.51	547.55	68.06	544.27
1308	1711.39	550.93	67.59	637.22
1351	2030.00	555.62	66.92	754.82
1395	2399.14	558.55	66.80	895.19
1478	3230.20	562.85	65.80	1196.30

# (b) 0.9 eV

T <sub>h</sub> (°C)	J <sub>SC</sub> (mA/cm <sup>2</sup> )	V <sub>OC</sub> (mV)	FF (%)	P <sub>mpp</sub> (mW/cm <sup>2</sup> )
856	47.99	595.66	81.67	23.34
940	82.55	611.02	83.56	42.15
1001	139.20	623.05	82.52	71.57
1072	217.91	635.06	82.12	113.65
1135	294.42	639.35	82.38	155.08
1153	335.99	645.56	80.73	175.10
1221	472.20	650.00	80.73	247.79
1241	494.79	654.93	80.69	261.49

1252	563.17	657.43	78.06	289.02
1303	708.55	659.63	79.65	372.26
1334	774.00	664.61	79.12	407.00
1344	856.32	663.61	79.01	448.96
1388	1037.03	667.83	77.69	538.01
1397	1076.50	667.55	77.44	556.47
1429	1229.81	670.27	77.37	637.7
1433	1248.00	671.36	78.44	657.24
1476	1476.74	673.98	75.76	754.01
1487	1543.80	674.54	75.00	780.73
1518	1729.90	676.30	73.62	861.28
1532	1818.90	677.59	73.81	909.72

(c) 1.1 eV

Th	$\mathbf{J}_{\mathbf{SC}}$	Voc	FF	P <sub>mpp</sub>
(°C)	(mA/cm <sup>2</sup> )	(mV)	(%)	(mW/cm <sup>2</sup> )
869	4.67	688.44	82.98	2.67
906	6.75	707.19	82.10	3.92
947	9.45	713.20	82.57	5.67
974	12.47	726.75	83.41	7.56
1012	17.07	732.25	83.88	10.48
1039	21.15	740.19	83.28	13.04
1083	29.40	749.85	84.20	18.56
1102	33.79	752.56	83.69	21.28
1159	49.56	764.45	83.64	31.69
1166	51.90	766.95	83.35	33.17
1235	78.98	775.65	82.98	50.83
1236	79.79	778.15	83.68	51.96
1282	103.47	784.88	81.16	65.913
1309	120.01	787.33	81.93	77.41
1316	124.50	791.51	83.57	82.35
1352	149.34	794.82	81.03	96.18
1357	154.81	797.83	82.50	101.90
1399	188.15	801.13	80.15	120.81
1409	198.07	804.22	79.87	127.22
1472	263.32	809.85	81.85	174.54
1519	322.43	817.40	76.73	202.23
1575	403.99	822.18	75.03	249.21
1631	499.00	828.78	73.43	303.67
1687	610.43	831.93	70.53	358.16

# S4.3. Bandgap offset voltage and voltage factor versus current density:

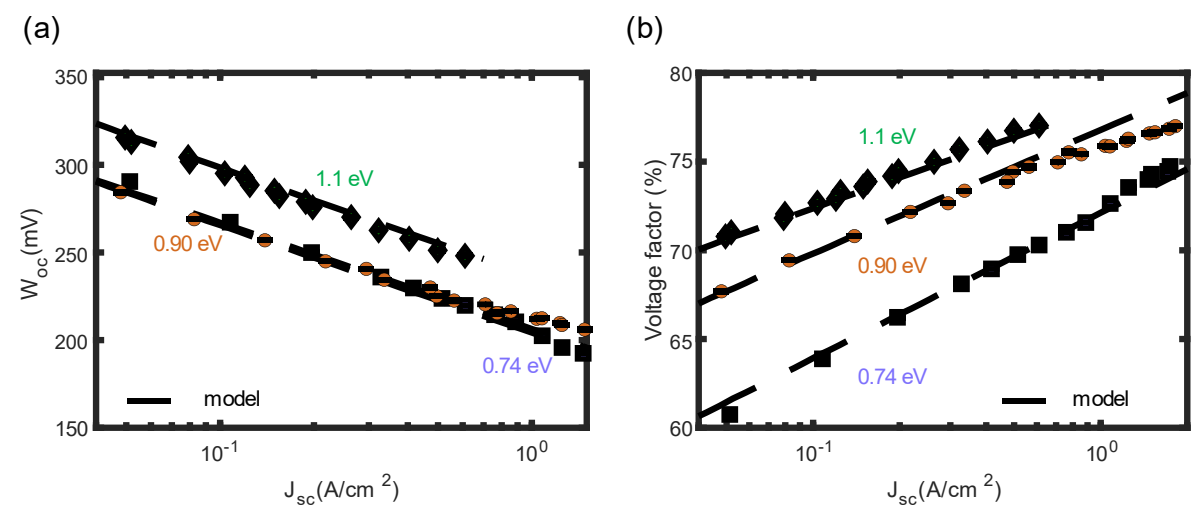


**Figure S4.3.** (a) Bandgap offset voltage  $W_{OC}$  and (b) voltage factor VF as a function of  $J_{sc.}$ 

## S4.4. Reproducibility of cell performance

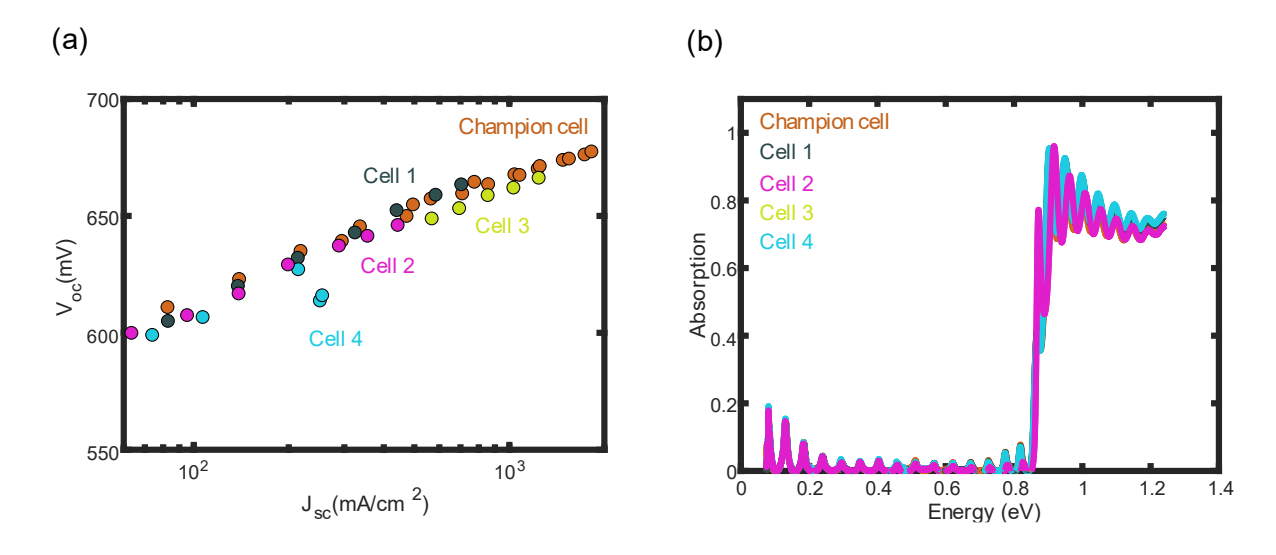


**Figure S4.4.** Characterization of five different 0.9 eV cells, showing reproducibility of key (a) electrical and (b) optical properties.

## S5. Additional analysis of the 0.74 eV and 1.1 eV cells

## S5.1. Comparisons to our prior InGaAs air-bridge cells reported in Ref. 16

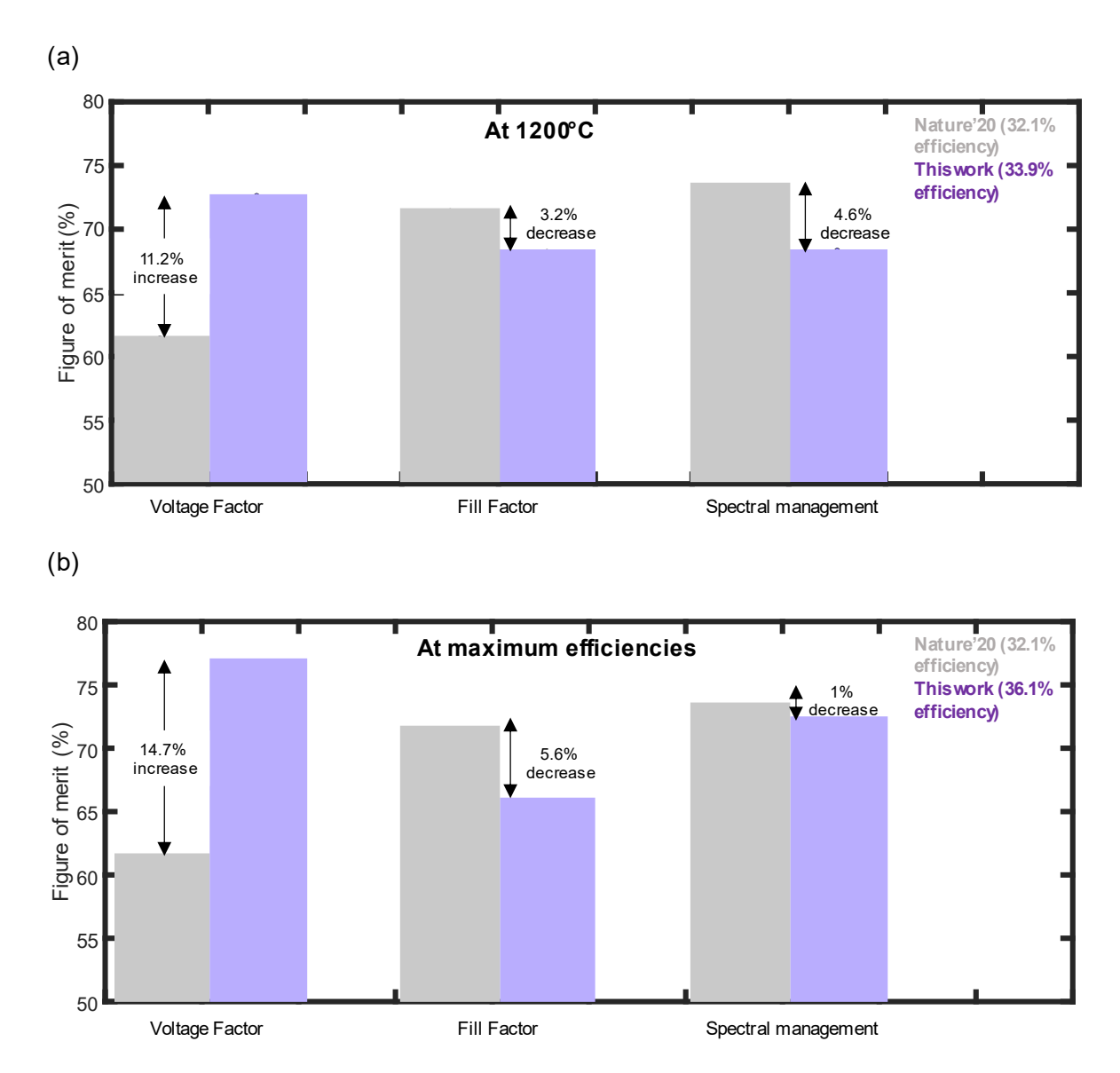


**Figure S5.1.** Efficiency breakdown comparing the 0.74 eV cell in this study to our previous work<sup>S5</sup> (a) under 1200°C illumination and (b) at their respective optimal emitter temperature. The analysis shows that the benefits of a higher voltage factor outweigh the negative effects of lower  $R_{out}$ . The difference in voltage can be attributed to the improved InP/InGaAs interface within the MOCVD grown epilayer compared to the previous MBE-grown layers.

# S5.2. Anticipated efficiency for the 1.1eV cell

Based on the validated model, the efficiency of the 1.1 eV cell will peak at 37.4% under 1700°C illumination. Improving the series resistance of this cell to 30 m $\Omega$ .cm<sup>2</sup> (comparable to the other two cells) can enhance efficiency to >41% at higher emitter temperatures.

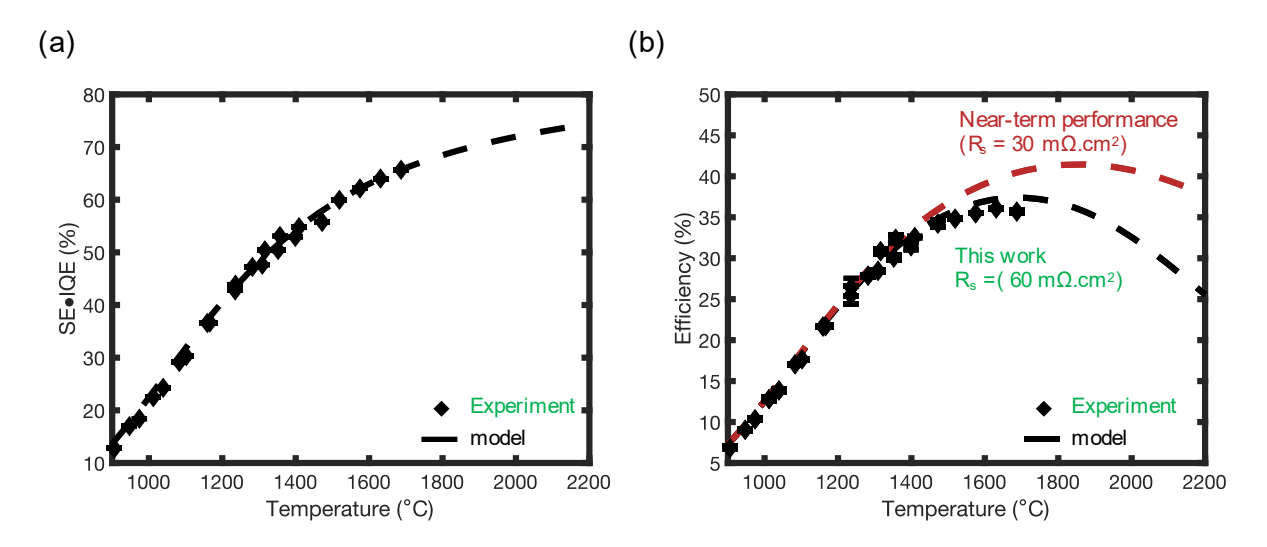


**Figure S5.2.** (a) Spectral management efficiency and (b) TPV efficiency of the 1.1 eV cell over an extended range of emitter temperatures.

## S6. Comparison to state-of-the-art TPV devices

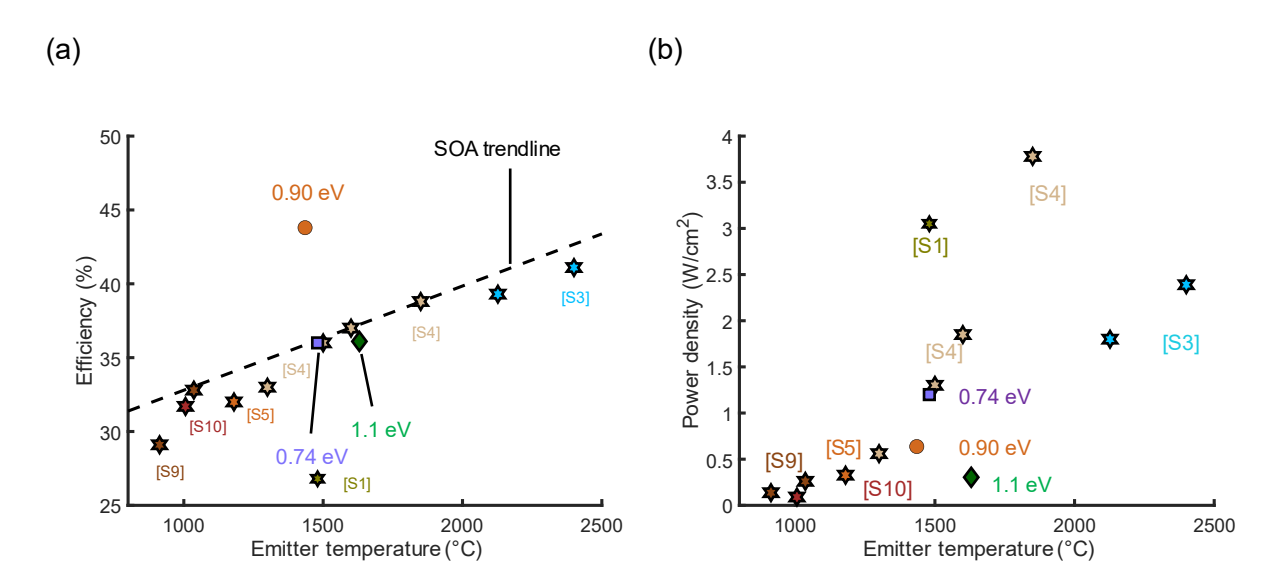


**Figure S6.** (a) Efficiency versus emitter temperature showing the maximum efficiencies for the three cells measured in this study compared to the state-of-the-art (SOA) TPV cells<sup>S1,S3-S5,S9,S10</sup> (star markers). The trendline is a best fit based on the SOA data shown and has been shifted upward to intercept the topmost data points. (b) Power density versus emitter temperature showing the maximum power density produced for the three cells measured in this study compared to the SOA TPV cells.

## S7. High view factor simulation for the 0.9 eV cell

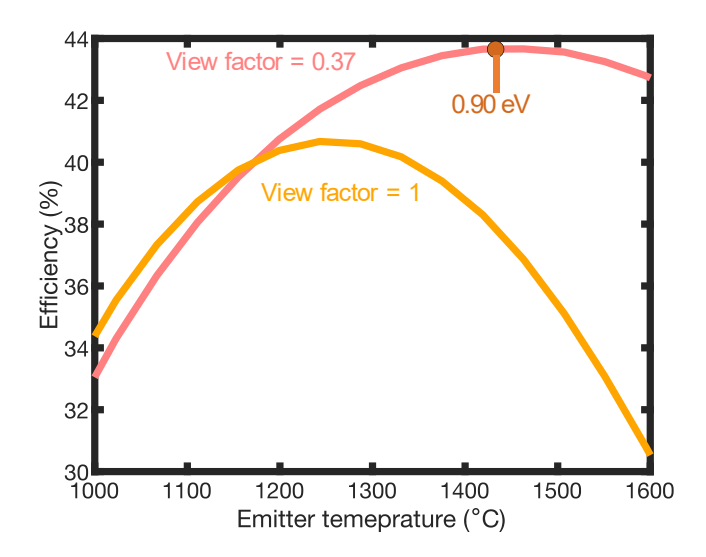


**Figure S7.** Simulated efficiency of the 0.9 eV cell versus emitter temperature for a view factor of 0.37 and 1. Assuming a view factor of 1, the 0.9 eV cell shows the highest efficiency at an emitter temperature of 1250°C.

#### S8. Emitter and cell characterization test station

#### S8.1. Emitter characterization

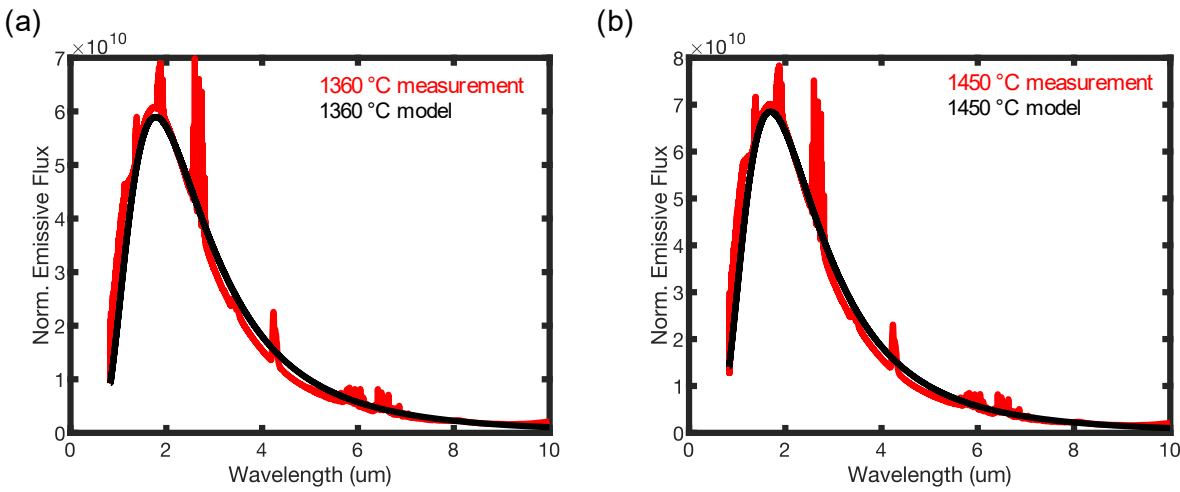


**Figure S8.1.** Emitter spectrum measurements and model for two representative temperatures of (a) 1360°C and (b) 1450°C. The emission spectra of the SiC emitter are measured with an FTIR spectrometer. Comparison to a blackbody spectrum yields an average thermal emittance of ~0.96, which, per the expression for effective emissivity, indicates that secondary reflections are negligible.

#### S8.2. Cell characterization station

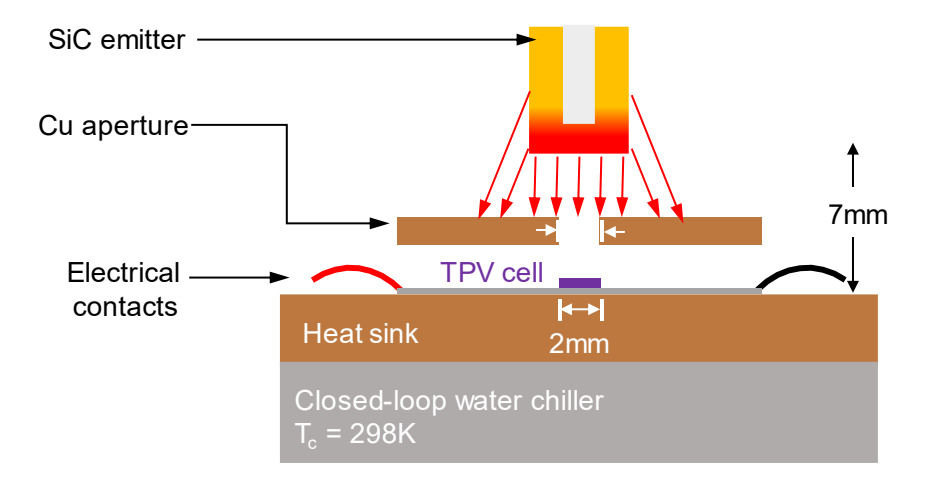


**Figure S8.2.** Electrical measurement of the TPV cell using a SiC globar as the emitter. The cell is placed on a heat sink connected to a chilled water loop.

# S8.3. Thermal management of the cell

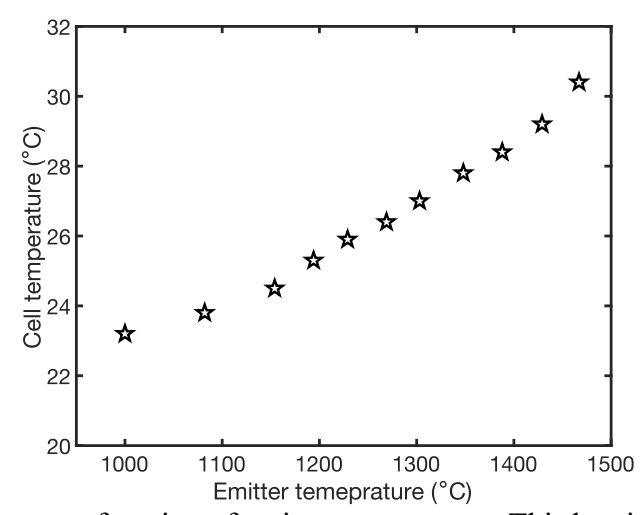


**Figure S8.3.** Cell heating as a function of emitter temperature. This heating effect is similar for all three cells measured in this study.

#### References

- S1. López, E., Artacho, I., and Datas, A. (2023). Thermophotovoltaic conversion efficiency measurement at high view factors. Solar Energy Materials and Solar Cells *250*, 112069. https://doi.org/10.1016/j.solmat.2022.112069.
- S2. Swanson, R.M. (1981). Recent Developments in Thermophotovoltaic Conversion. In Photovoltaic Solar Energy Conference, W. Palz, ed. (Springer Netherlands), p. 1097.
- S3. LaPotin, A., Schulte, K.L., Steiner, M.A., Buznitsky, K., Kelsall, C.C., Friedman, D.J., Tervo, E.J., France, R.M., Young, M.R., Rohskopf, A., et al. (2022). Thermophotovoltaic efficiency of 40%. Nature 604, 287–291. 10.1038/s41586-022-04473-y.
- S4. Tervo, E.J., France, R.M., Friedman, D.J., Arulanandam, M.K., King, R.R., Narayan, T.C., Luciano, C., Nizamian, D.P., Johnson, B.A., Young, A.R., et al. (2022). Efficient and scalable GaInAs thermophotovoltaic devices. Joule *6*, 2566–2584. https://doi.org/10.1016/j.joule.2022.10.002.
- S5. Fan, D., Burger, T., McSherry, S., Lee, B., Lenert, A., and Forrest, S.R. (2020). Near-perfect photon utilization in an air-bridge thermophotovoltaic cell. Nature *586*, 237–241. 10.1038/s41586-020-2717-7.
- S6. Omair, Z., Scranton, G., Pazos-Outón, L.M., Xiao, T.P., Steiner, M.A., Ganapati, V., Peterson, P.F., Holzrichter, J., Atwater, H., and Yablonovitch, E. (2019). Ultraefficient Thermophotovoltaic Power Conversion by Band-Edge Spectral Filtering. Proc. Natl. Acad. Sci. U. S. A. 116, 15356.
- S7. Lee, B., Lentz, R., Burger, T., Roy-Layinde, B., Lim, J., Zhu, R.M., Fan, D., Lenert, A., and Forrest, S.R. (2022). Air-Bridge Si Thermophotovoltaic Cell with High Photon Utilization. ACS Energy Lett 7, 2388–2392. 10.1021/acsenergylett.2c01075.
- S8. Cabrera, A., Ramos, A., Artacho, I., Gomez, M., Gavin, K., Martí, A., and Datas, A. (2018). Thermophotovoltaic efficiency measurement: design and analysis of a novel experimental method. 1–4.
- S9. Burger, T., Roy-Layinde, B., Lentz, R., Berquist, Z.J., Forrest, S.R., and Lenert, A. (2022). Semitransparent thermophotovoltaics for efficient utilization of moderate temperature thermal radiation. Proceedings of the National Academy of Sciences *119*, e2215977119. 10.1073/pnas.2215977119.
- S10. Lim, J., Roy-Layinde, B., Liu, B., Lenert, A., and Forrest, S.R. (2023). Enhanced Photon Utilization in Single Cavity Mode Air-Bridge Thermophotovoltaic Cells. ACS Energy Lett 8, 2935–2939. 10.1021/acsenergylett.3c00720.